Dependence of scrape-off layer profiles and turbulence on gas fuelling in high density H-mode regimes in TCV

A. Stagni[1], N. Vianello[1], C.K. Tsui[2], C. Colandrea[3], S. Gorno[3], M. Bernert[4], J.A. Boedo[3], D. Brida[4], G. Falchetto[5], A. Hakola[6], G. Harrer[7], H. Reimerdes[3], C. Theiler[3], E. Tsitrone[5], N. Walkden[8], the TCV Team[a] and the EUROfusion MST1 Team[b]

[1]Consorzio RFX (CNR, ENEA, INFN, Università di Padova, Acciaierie Venete SpA), Corso Stati Uniti 4, 35127 Padova, Italy

[2]University of California San Diego, Center for Energy Research, La Jolla, California 92093, USA

[3]École Polytecnique Fédérale de Lausanne, Swiss Plasma Center, CH-1015 Lausanne, Switzerland

[4]Max-Planck-Institut für Plasmaphysik, Boltzmannstrasse 2, D-85748 Garching bei München, Germany

[5]CEA, IRFM, F-13108 Saint-Paul-lez-Durance, France

[6]VTT Technical Research Centre of Finland Ltd., PO Box 1000, FI-02044 VTT, Finland

[7]Institute of Applied Physics, TU Wien, Fusion@ÖAW, Wiedner Hauptstr. 8-10, 1040 Vienna, Austria

[8]CCFE, Culham Science Centre, Abingdon, Oxon, OX14 3DB, United Kingdom

[a]See author list of H. Reimerdes et al 2022 *Nucl. Fusion* **62** 042018

[b]See author list of B. Labit et al 2019 *Nucl. Fusion* **59** 086020

E-mail: adriano.stagni@igi.cnr.it

Abstract. A set of high density, highly shaped H-mode discharges has been performed in the TCV tokamak with the aim of assessing the effects of increasing divertor neutral recycling on the properties of upstream inter-ELM scrape-off layer (SOL) profiles and transport. An increase of divertor neutral pressure has been correlated with the evolution of separatrix properties and turbulence level. The latter has been quantified by means of the α_t parameter introduced in [1], describing the contribution of resistive-interchange turbulence in the SOL relative to drift wave transport. The analysis reveals a general broadening of the upstream SOL profiles as α_t increases, with the SOL power width measured by the vertical IR thermography system increasing significantly. In a similar way, the upstream density profile widens in the near SOL, whereas in the far SOL a density shoulder is observed to progressively form and increase in amplitude. This behaviour is associated with an enhancement of far SOL turbulent transport in the form of blob-filaments travelling radially faster across the far SOL and becoming bigger at higher α_t. The detected filaments, evaluated from the fast reciprocating probe at the outer midplane, are determined to mostly belong to the Resistive Ballooning and Resistive X-point regimes.

Keywords: H-mode, ELMs, QCE, scrape-off layer, e-folding lengths, blob-filaments
To be Submitted to: *Nucl. Fusion*

1. Introduction

Unravelling the physical mechanisms underlying the transport of particles and power in the edge and scrape-off layer (SOL) regions of a tokamak is of utmost importance in view of safe and reliable operation of future fusion devices like ITER. Due to engineering constraints on material survival towards tungsten recrystallization, excessive erosion and melting, an upper boundary of 10 MW/m^2 is imposed on the peak heat flux transported towards the divertor targets [2], and even lower for the ITER beryllium first wall plasma-facing components. This limit acquires even more relevance when considering that ITER, in its baseline scenario [3], will operate in a low-collisionality H-mode confinement regime characterised by the presence of type-I edge-localised modes (ELMs) imposing large transient heat loads which, if uncontrolled, will cause severe material damage or component failure.

For this reason, in ITER a large fraction of the power crossing the separatrix must be removed by volumetric radiation in the SOL and divertor regions. This demand, coupled with the ultimate objective of attaining reactor-relevant core plasma performances with maximization of the fusion reaction rate, calls for high-density operational regimes in ITER and future fusion devices characterized by both high neutral recycling and partial divertor detachment. In particular, the former has been found to strongly influence the upstream density profile evolution in terms of achieved separatrix density [4] and SOL profile modification with formation of a *density shoulder*, both in L-mode [5, 6, 7, 8, 9, 10] and in H-mode [11, 12, 13, 14].

Along with being key for achieving high SOL radiative losses, high separatrix density has been identified as a necessary condition for accessing some types of H-mode scenarios in which large type-I ELM bursts are replaced by smaller ELMs [15, 16]. These regimes have been recently denoted as *quasi-continuous exhaust* (QCE) [13], being generally associated with an increase of filament activity in the far SOL [17, 14] and an ELMy behaviour characterised by low-amplitude, high-frequency incoherent bursts. While the density and temperature profiles in the QCE regime are still characterized by the presence of an H-mode pedestal near the separatrix, the SOL power width has been found to increase up to L-mode-like values at the highest gas fuelling levels [13]. The transition from type-I to small ELMs at increasing fuelling level is not abrupt but rather proceeds gradually with a progressive increase of the SOL power width, therefore providing a possible way of relieving the divertor target heat load all the while preserving an H-mode level of confinement. On the other hand, filaments can be held up responsible for a significant part of the cross-field transport in the SOL [18], thereby an enhancement of filamentary radial convective transport at the outer midplane (OMP) registered in high-density H-mode may pose a risk for first wall safety.

The progressive modification of upstream profiles, both in the near and far SOL, at increasing divertor neutral pressure and the associated transition towards more dissipative regimes have been addressed on a theoretical ground in a recent paper by Eich *et al* [1], leveraging previous models by Rogers, Drake and Zeiler [19] and Scott [20, 21]. In these works a description of the SOL transport regimes has been attempted based on few dimensionless parameters assessing the relative strength of different transport mechanisms. Within the three-dimensional drift-Alfvén (DALF3) turbulence model [20] two parameters are identified, namely the curvature drive

$$\omega_B = \frac{2\lambda_p}{R}\left(1+\frac{1}{\bar{Z}}\right) \tag{1}$$

setting the strength of interchange turbulence arising from magnetic curvature, and the normalized collisionality

$$C = 0.51\nu_{ei}\frac{\lambda_p}{c_s}\frac{m_e}{M_i}\left(\frac{q_{cyl}R}{\lambda_p}\right)^2 \tag{2}$$

with λ_p the separatrix pressure e-folding length, R the tokamak major radius, $q_{cyl} = \frac{B_T}{\langle B_{pol}\rangle}\frac{\hat{\kappa}}{A}$ the cylindrical safety factor, $A = R/a$ the inverse aspect ratio, $\langle B_{pol}\rangle = \frac{\mu_0 I_p}{2\pi a\hat{\kappa}}$ the poloidally-averaged separatrix poloidal magnetic field. Both parameters, firstly defined in [20], have been generalized in [1] for arbitrary plasma composition by means of the average ion charge $\bar{Z} = n_e/\sum_j n_j$ and the effective ion mass $M_i = (\sum_j n_j M_j)/n_e$. In the same work, geometrical effects linked to non-circularity of the separatrix are taken into account through the factor $\hat{\kappa} = \sqrt{[1+\kappa_{geo}^2(1+2\delta^2-1.2\delta^3)]/2}$.

Based on equations 1 and 2, a turbulence control parameter has been defined in [1]:

$$\alpha_t = C\omega_B = q_{cyl}^2 R\sqrt{\frac{m_e}{M_i}}\left(1+\frac{1}{\bar{Z}}\right)\frac{1.02\sqrt{2}e^4\ln\Lambda n_e}{12\pi^{3/2}\epsilon_0^2 T_e^2}Z_{eff}f_{Z_{eff}} \tag{3}$$

being $\ln\Lambda$ the Coulomb logarithm, $Z_{eff} = (\sum_j n_j Z_j^2)/n_e$ the effective ion charge and $f_{Z_{eff}}$ a function defined in [1] accounting for a $Z_{eff} > 1$ modification of the numerical factor in the Braginskii electron resistivity for singly-charged ion species. The α_t parameter has been shown through simulations to regulate the strength of the resistive-interchange turbulence relative to drift-wave transport by setting the phase shift between the potential and electron pressure fluctuations [22]. In particular, drift waves dominate the SOL transport when $\alpha_t \approx 0$, whereas they are overtaken by interchange turbulence when $\alpha_t \gtrsim 1$. In support to the proposed theoretical framework, recent experiments carried out on ASDEX-Upgrade discharges have shown that the SOL power channel widens significantly in H-mode conditions as α_t increases at higher fuelling [1, 13].

The present work reports on an experimental activity carried out on the *Tokamak à Configuration Variable* (TCV) [23], with the aim of shedding light on the relationship between the divertor recycling state and the properties of upstream SOL profiles and turbulence. Within high-density H-mode scenarios, including but not limited to QCE, the divertor neutral pressure is scanned by changing the gas fuelling level and subsequently correlated with the α_t parameter through the variation of separatrix density. Afterwards, the impact on the upstream SOL plasma is addressed in terms of

broadening in the near SOL power width and density e-folding length, far SOL density shoulder formation and increase of filamentary transport.

The paper is structured as follows. After a brief overview in section 2 of the device setup, the diagnostics used and the considered scenario, in section 3 a description will be given of the workflow adopted in order to properly evaluate the separatrix position and, as a consequence, the main separatrix profile parameters. In section 4 the results of the present analysis are reported linking the divertor neutral pressure, the α_t parameter and the modification of SOL profiles, whereas the impact on filamentary transport is assessed in section 5. Finally, conclusions will be drawn in section 6 together with future developments.

2. Experimental setup

2.1. Machine and diagnostics

TCV is a medium-sized tokamak located at the Swiss Plasma Center (EPFL, Lausanne, Switzerland), with a major radius $R = 0.88$ m and minor radius $a = 0.25$ m. With its highly elongated vessel and 16 independently powered poloidal field coils, this device is particularly suitable for achieving a wide range of plasma shapes and divertor geometries, spanning large intervals of elongation ($\kappa \leq 2.8$) and triangularity ($-0.7 \leq \delta \leq 1$). A set of removable baffles has been installed starting from the 2019 experimental campaigns [24, 25], with the main aim to reduce the coupling between the core plasma and the divertor neutrals while still being compatible with a wide range of divertor configurations.

A typical magnetic equilibrium considered in this work is shown in figure 1, together with the vessel geometry and the analysed diagnostics. Fuelling has been achieved by D_2 gas puffing from either the top or the outermost floor piezoelectric valves [26], shown in figure 1*a* as black rectangles. In the same figure the two vertical yellow lines indicate the core and edge chords of a Far-InfraRed (FIR) interferometer, measuring line-averaged electron densities. The red dots and lines indicate, respectively, the Thomson Scattering (TS) measurement volumes and lines of sight [27]. The green patch shows the position of the divertor baratron, measuring the pressure of neutral particles in the divertor region. In figure 1*b* the lines of sight of 64 gold foil bolometers are shown, whose measurements are tomographically inverted so as to infer the radiated power [28]. In figure 1*c* the cyan region indicates the typical useful field of view of a Vertical InfraRed (VIR) thermography system used to measure the floor tiles temperature around the Outer Strike Point (OSP) [29]. The blue dots represent an array of wall-embedded Langmuir Probes (LPs), recently upgraded in order to attain full poloidal coverage of the tokamak's first wall [30, 31]. In the discharges considered for this work they have been operated with a triangular voltage sweep in order to obtain measurements of electron density and temperature profiles at the first wall and divertor target. A fast reciprocating probe (RCP) [32, 33], whose location is indicated in figure 1*c* with a black rectangle at the

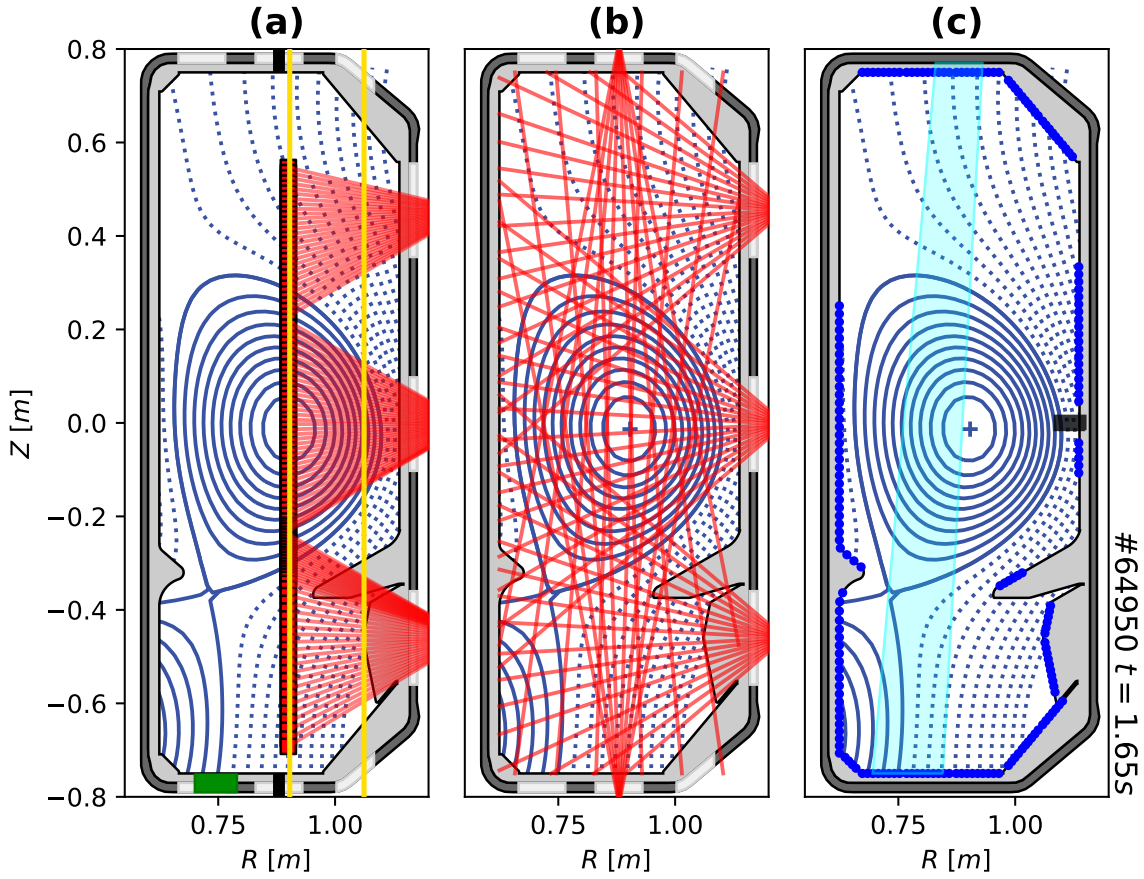

Figure 1: Diagnostics, vessel geometry and typical plasma geometry considered in this work. (a) Red lines and dots indicate Thomson Scattering volumes and lines of sight respectively, while the yellow lines indicate the core and edge interferometer chords. The green patch represents the divertor neutral pressure baratron. The locations of the piezoelectric gas valves are indicated in black. (b) Bolometry lines of sight are shown in red. (c) The cyan region represents the typical portion of the Vertical InfraRed camera field of view used for calculation of the perpendicular heat flux. Langmuir probes are shown as blue dots, whereas the black patch at the machine outer midplane indicates the position of the fast reciprocating probe.

OMP, plunges once per discharge providing further measurements of upstream electron density and temperature through a double probe arrangement. Another electrode on the RCP head measures the ion saturation current with a high time resolution, while the remaining ones, yielding measurements of floating potential, are displaced poloidally and radially so that electric field fluctuations in both the perpendicular directions can be inferred.

2.2. Scenario

The database considered in this work consists of several high-density H-mode discharges in baffled vessel configuration with a highly shaped lower single null magnetic equilibrium, shown in figure 1. The main discharge parameters are plasma current $I_p = 170$ kA, toroidal magnetic field on axis $B_T = 1.4$ T. The direction of the toroidal field is chosen in such a way that the ion $\mathbf{B} \times \nabla B$ drift points towards the active X-point for favourable H-mode access. The plasma elongation is $\kappa_{geo} \sim 1.5$, while the upper and lower triangularities are respectively $\delta_{up} \sim 0.4$ and $\delta_{low} \sim 0.6$. In order to access H-mode, an additional heating power of ~ 1 MW has been provided by co-current Neutral Beam Injection (NBI) [34] between 0.8 s and 1.8 s in all considered pulses, as shown in figures 2*a*-*b*. Gas fuelling from either the top or the bottom valves has been carried out in feed-forward from 0.9 s until the end of the discharge, either as two consecutive steps (e.g. as in figure 2*c*) or as a step followed by a ramp (e.g. as in figure 2*d*), in order to produce a scan in divertor neutral pressure $p_{n,div}$ spanning an interval between ~ 20 mPa and ~ 120 mPa (see figures 2*e*-*f* for reference). Correspondingly, the edge line-averaged density varies between $\sim 3 \cdot 10^{19}$ m^{-3} (edge Greenwald fraction [35] $f_{Gw} \sim 0.25$) and $\sim 7 \cdot 10^{19}$ m^{-3} ($f_{Gw} \sim 0.63$). As a result of the increase in divertor neutral pressure, the ELM behaviour as seen from a photodiode registering the D_α light emission along a vertical line of sight is largely modified (see figures 2*i*-*j*), transitioning from well-defined type-I ELMs at low $p_{n,div}$ towards a small ELM/QCE regime at higher fuelling. In turn, as shown in figures 2*k*-*l*, the energy confinement is worsened at higher divertor neutral pressure remaining however on H-mode levels even at the highest densities during the whole NBI-heated phase, with a reduction of $H_{98(y,2)}$ from ~ 1.2 to ~ 1.

3. Methodology

The separatrix parameters for evaluation of transport and profile properties are estimated from TS density and temperature measurements, combined with RCP data when available during the corresponding plunge time intervals. All data are remapped to the outer midplane in $s = R - R_{sep}$ and $\rho_\psi = \sqrt{(\psi - \psi_0)/(\psi_1 - \psi_0)}$ coordinates through the equilibrium reconstruction code LIUQE [36], where s is the distance from the separatrix at the OMP, R_{sep} is the separatrix outer midplane radius, ρ_ψ is the normalized poloidal magnetic flux coordinate, ψ_0 and ψ_1 the poloidal magnetic flux function evaluated at the magnetic axis and at the separatrix, respectively.

During type-I ELMy phases the profiles have been taken in 200-250 ms time intervals considering a 65-95% inter-ELM cycle range. On the other hand no ELM filtering was applied during small ELM/QCE phases, since no clear identification of ELMy behaviour from the D_α signal was possible, with the profiles being evaluated in a 120-150 ms time range. The resulting measured data points have been fitted by using a composite piecewise function made of a fourth-order polynomial for the core region and a modified hyperbolic tangent function [37] for the edge-SOL region, similarly to

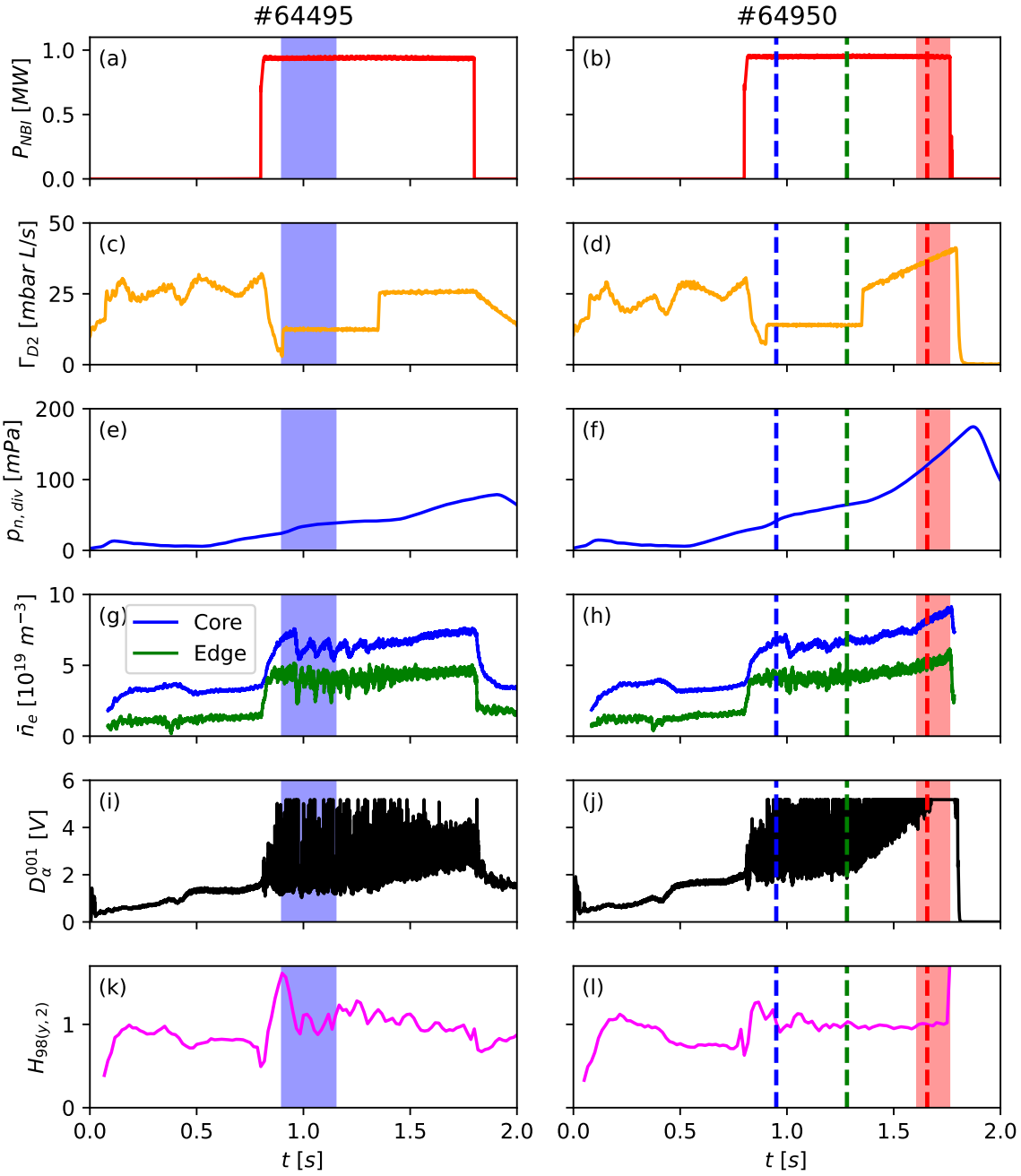

Figure 2: Time evolution of the net input NBI power (a)-(b), D_2 gas flow rate (c)-(d), divertor neutral pressure (e)-(f), core and edge line-averaged densities (g)-(h), D_α light emission from a vertical line of sight (i)-(j), $H_{98(y,2)}$ confinement factor (k)-(l) for two sample discharges in the considered database.

the procedure described in [38]. Constraints on continuity and differentiability of the resulting fitting function have been imposed at the contact point between the two pieces, established at $s = -5$ cm or equivalently $\rho_\psi \sim 0.75$ for all profiles, as well as a constraint of null derivative at the magnetic axis. Limited to the density profile the fitting model has been given a finite constant negative slope immediately after the pedestal in order to well reproduce the overall decreasing far SOL density measurements.

In presence of a steep edge H-mode pedestal gradient the assessment of the plasma parameters at the separatrix becomes extremely sensitive to its position. Since the latter can be inferred from the equilibrium reconstruction only within an accuracy of a few mm, a direct evaluation would yield too large uncertainties on the values of separatrix density and temperature. Therefore, throughout this work the separatrix position is determined from an estimation of the corresponding temperature based on energy balance between the power crossing the separatrix into the SOL and that flowing along the open magnetic field lines towards the divertor target. The former is given by

$$P_{SOL} = P_\Omega + P_{NBI} - P_{rad,core} \tag{4}$$

with P_Ω the Ohmic heating power, P_{NBI} the total NBI power coupled to the plasma (net of beam losses) and $P_{rad,core}$ the core radiated power. Under the assumption of conduction-dominated parallel transport, the two-point model by Stangeby [39] predicts a separatrix temperature of

$$T_{e,sep} \approx \left(T_{e,t}^{7/2} + \frac{7}{4} \frac{P_{SOL} L_\parallel}{A_{SOL} \kappa_{0e}} \right)^{2/7} \tag{5}$$

where $L_\parallel \sim \pi q_{cyl} R$ is the upstream-to-target connection length and $A_{SOL} \sim 4\pi R \langle \lambda_q \rangle \frac{\langle B_{pol} \rangle}{B_T}$ is the SOL wetted surface area, with $\langle \lambda_q \rangle$ the poloidally-averaged SOL power width [40] estimated from the VIR thermography measurements (see section 4.1). The electron parallel heat conduction constant κ_{0e} is corrected according to [41] in order to account for the effect of $Z_{eff} > 1$, with the effective ion charge estimated from the determination of the neoclassical resistivity and bootstrap current as described in [42, 43]. The resulting expression for the separatrix temperature is

$$T_{e,sep} \approx \left(\frac{7}{16} \frac{P_{SOL} q_{cyl}^2 A}{\kappa_{0e} \hat{\kappa} \langle \lambda_q \rangle} \right)^{2/7} . \tag{6}$$

The target temperature $T_{e,t}$ has been dropped altogether from equation 6 since, as shown in figure 3*a*, its value measured at the OSP by floor Langmuir probes is $T_{e,t} \approx 10$ eV whereas the evaluation of equation 6 typically yields $T_{e,sep} \approx 50$ eV in TCV [44]. On the other hand this observation can serve as an indication of high-recycling attached divertor conditions, together with the floor LPs measurements of integrated ion flux in figure 3*b* showing no clear sign of rollover with increasing fuelling.

In the end, the upstream temperature profiles have been shifted rigidly in order to match the separatrix estimation and the density profiles have been shifted by the same amount, since measured on the same coordinate basis, for assessment of the separatrix density. Throughout the whole database a radial shift of $\Delta\rho_\psi = (-5.6 \pm 3.8) \cdot 10^{-3}$,

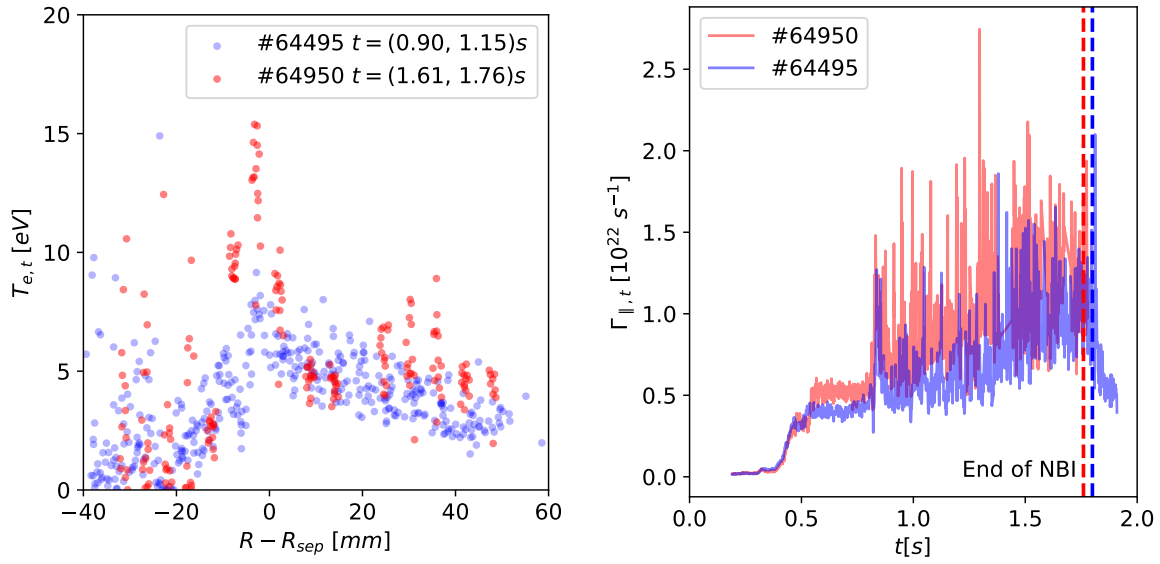

(a) (b)

Figure 3: Langmuir probes measurements of (a) upstream-remapped outer target temperature during two time intervals and (b) time evolution of the total inter-ELM integrated floor ion flux, for discharges #64495 and #64950. The two profiles in panel (a) have been evaluated during the time intervals highlighted with corresponding colors in figure 2, with ELM filtering being performed only for the time interval of discharge #64495.

or equivalently $\Delta s = (-1.5 \pm 1.1)$ mm is observed with respect to the LIUQE reconstruction. Examples of kinetic profiles for the present database are given in figure 4, comprehensive of both measured data points and the associated fitting curves. It should be pointed out that a larger scatter is present in the density signal acquired by the TS system during QCE phases with respect to type-I ELM regimes, given that any small ELM fluctuation is retained due to the lack of a filtering procedure. Nevertheless a reliable determination of the density profiles is still possible even during QCE, with the fitting quality remaining high. At increasing divertor recycling the temperature profiles are significantly affected only in terms of decreasing pedestal height and a lower pedestal slope in the vicinity of the separatrix, whereas the separatrix temperature is approximately constant at $T_{e,sep} = (46.5 \pm 3.3)$ eV throughout the database, similarly to the estimate given in [44]. Conversely, a global upwards vertical shift can be seen in the density profile when moving towards higher neutral recycling, with a higher pedestal top and separatrix density achieved.

Extending this last observation to the whole database, in figure 5 the global trends of the estimated separatrix density (on the left) and the α_t parameter (on the right) are shown. Points with an uncertainty bigger than their absolute value have been discarded, nevertheless some still remain on the right panel with a rather large standard deviation,

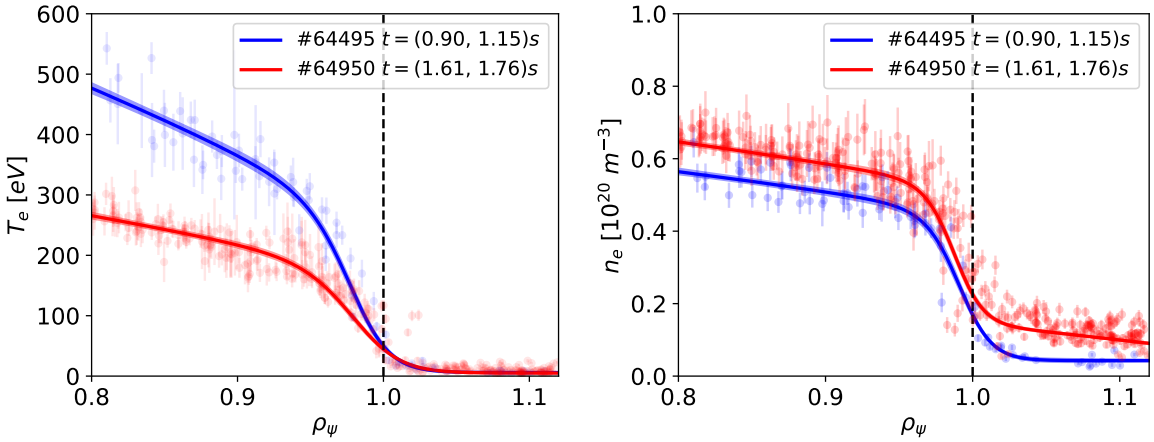

Figure 4: Upstream edge-SOL electron temperature (left) and density (right) profiles for the considered sample discharges during the two time intervals highlighted with corresponding colors in figure 2. The TS and (for the red case) RCP data are shown as semi-transparent points with their associated error bars. The solid curves represent the *mtanh* part of the fitting model, while the shaded regions indicate the uncertainty estimate of the fit. Both data and fits have been shifted along the radial coordinate in order to match their respective $T_{e,sep}$ estimation in equation 6. The separatrix position has been represented through a dashed black vertical line.

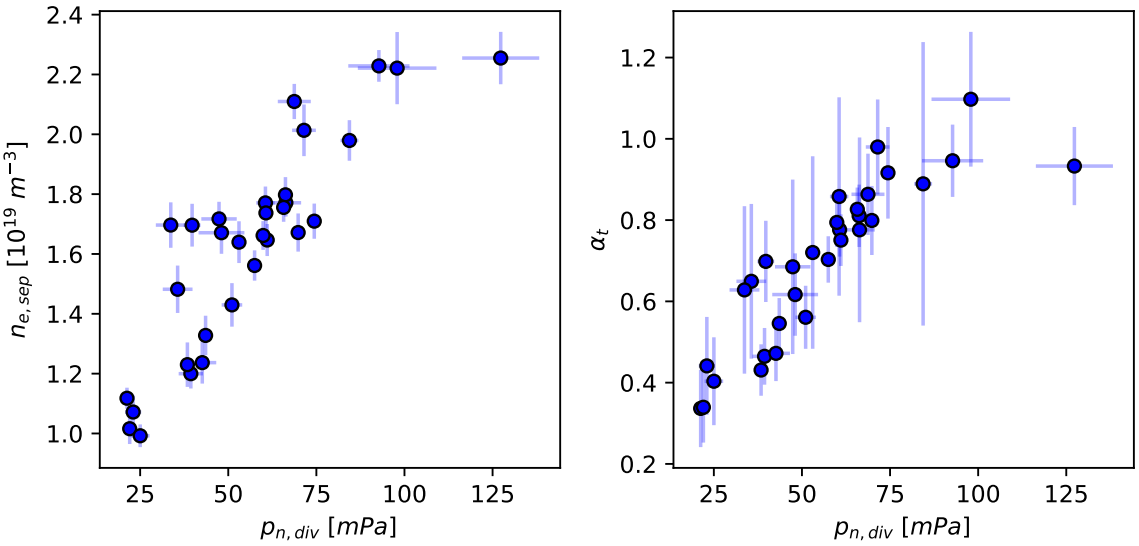

Figure 5: Dependence on the divertor neutral pressure $p_{n,div}$ of (left) the separatrix density $n_{e,sep}$ and (right) the interchange turbulence parameter α_t for the database analysed for this work.

probably due to being associated with particularly noisy signals from the VIR camera. Due to the little impurity concentration, $\bar{Z} \sim 1$ and $M_i \sim 2m_p$ have been used for proper evaluation of α_t while retaining the dependence on Z_{eff}. As is to be expected, the separatrix density increases at higher divertor neutral pressure, until saturation occurs at $\sim 2.3 \cdot 10^{19}$ m^{-3} at around 90 mPa. Whether this saturation can be ascribed to efficient neutral compression in the divertor region at high $p_{n,div}$ due to the presence of the long LFS baffle will be the subject of further investigation comparing this dataset with a similar one in unbaffled vessel configuration. The α_t parameter follows closely the behaviour of the separatrix density, suggesting that at higher fuelling the profiles around the separatrix become more interchange-unstable, leading to enhanced transport into the SOL.

4. Evolution of the upstream SOL profiles

4.1. Heat flux profile broadening

Firstly, the behaviour of the parallel heat flux profile is investigated as the divertor evolves towards a more dissipative state by increasing gas fuelling. For this purpose, VIR thermography measurements are exploited to obtain an estimate of the SOL power fall-off length. The outer target perpendicular heat load is first deduced from the floor tile temperature distribution using the THEODOR code [45, 46] and subsequently converted to upstream parallel heat flux, accounting for target field line grazing angle and upstream-to-target total magnetic flux expansion [47]. Each of the measured profiles are first ELM-filtered during type-I ELMy phases as described in section 3, then individually fitted by means of an Eich function [40]. For a given time interval the upstream λ_q is obtained by time-averaging the values obtained for each fit, weighted on the inverse of their uncertainty. The corresponding poloidally averaged quantity appearing in equation 6 is obtained by remapping the OMP estimation as in [40].

In figure 6 the discharge #64950 is examined at the three different times indicated with vertical lines in the left panels of figure 2. The corresponding parallel heat flux profiles are shown, each one being associated with their respective values of $p_{n,div}$ as well as the Eich fit estimations of decay length λ_q and divertor spreading S. The background heat fluxes inferred from the fitting procedure are subtracted from each of the three profiles, so that they can be compared on a common baseline. As the divertor neutral pressure increases, the heat flux profile undergoes a clear broadening with a significant increase of the SOL power fall-off length, up to a factor of ~ 1.5 during the considered discharge, and a corresponding reduction of the peak heat flux. This trend is retained globally over the entirety of the database as shown in figure 7, with the poloidally-averaged SOL power width steadily increasing at higher fuelling, up to a factor ~ 2.5 within the attained α_t parameter interval.

In recent years a number of scaling laws have been published for the description of the SOL power width during inter-ELM phases of type-I ELMy H-mode regimes.

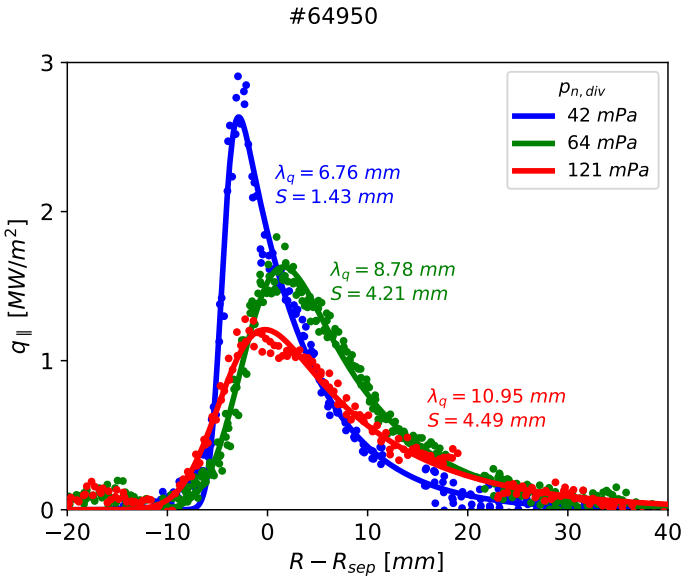

Figure 6: Inter-ELM target parallel heat flux profiles, mapped upstream, at three different times during discharge #64950, together with their respective estimated λ_q and S parameters. The chosen times, which have been associated with corresponding values of divertor neutral pressure in the legend, are represented in the left panels of figure 2 with corresponding colors. The background heat fluxes estimated from the Eich fit have been subtracted for all profiles.

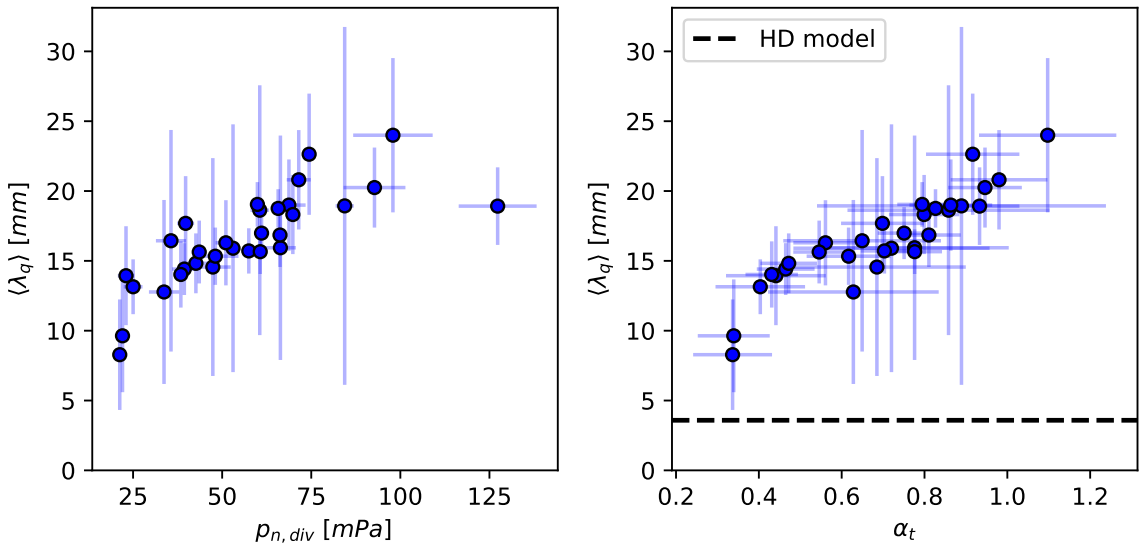

Figure 7: Dependence of the poloidally-averaged SOL power fall-off length on the divertor neutral pressure (left) and the α_t parameter (right). On the right panel, the low-collisionality heuristic-drift model prediction is represented by means of the dashed black horizontal line.

In particular, within an extensive multi-machine experimental activity measuring the divertor target heat flux profile through IR cameras [48] the SOL power width was shown to be primarily determined by the inverse of the poloidal magnetic field at the OMP, without any explicit dependence on machine size:

$$\lambda_q \sim 0.63 \cdot B_{pol,OMP}^{-1}. \tag{7}$$

A heuristic-drift (HD) model based on neoclassical ion drifts [49, 50] is able to explain the experimentally observed parameter dependencies (or lack thereof) through the relation

$$\langle \lambda_q \rangle \sim 1.6 \frac{a}{R_0} \rho_{s,pol} \tag{8}$$

where $\rho_{s,pol} = \sqrt{M_i T_{e,sep}}/(e\langle B_{pol} \rangle)$ is the poloidal ion sound Larmor radius, proportional to the inverse of the poloidally-averaged poloidal magnetic field. Both the empirical and the theoretical scaling laws however refer to low separatrix collisionality conditions, much unlike those observed throughout the present analysis in which α_t ranges from a minimum of ~ 0.3 to a maximum of ~ 1. In addition, while on one hand this scaling manages to well reproduce the experimental results of a zero gas puff multi-machine database [48, 50], on the other hand it has been shown to overestimate TCV data to some extent [51], so that equation 8 can be treated at least as an upper boundary for the low collisionality SOL power width. As a consequence, as shown in the left panel of figure 7 the attained $\langle \lambda_q \rangle$ values are always above the HD model prediction of ~ 3.6 mm with the typical parameters $a \sim 0.22$ m, $R_0 \sim 0.9$ m, $\rho_{s,pol} \sim 9.2$ mm observed in this database. Moreover, the lowest $\langle \lambda_q \rangle \sim 8$ mm (i.e. $\lambda_{q,OMP} \sim 4.4$ mm) achieved in this analysis is higher than the biggest SOL width obtained within the zero-fuelling database of [51], considering discharges with similar input parameters to those used in this analysis. The broadening of the SOL width with respect to the low-collisionality reference value is well correlated with the increase of α_t, therefore suggesting that the progressive destabilization of resistive-interchange modes near the separatrix as the density increases with the divertor neutral pressure might produce a larger SOL power channel, coherently with ASDEX-Upgrade observations [1].

4.2. Density shoulder formation

The formation of a density shoulder feature in the upstream density profiles has been already observed in L-mode conditions to be often associated with the onset of target ion flux rollover, further developing after divertor detachment [8, 9, 10]. On the other hand this requirement is relaxed in H-mode conditions, where achievement of a high-recycling divertor without a proper rollover has been sufficient for shoulder formation [14]. In the present section the mentioned studies are extended, reporting in more detail on the role of the divertor neutral pressure in setting the shape of the upstream density profiles both in the near and far SOL regions.

In figure 8 the same upstream density profiles presented in the right panel of figure 4 are shown, with both the diagnostics data and the fitting curves normalized to their respective separatrix density values and a logarithmic vertical scale, in order to highlight

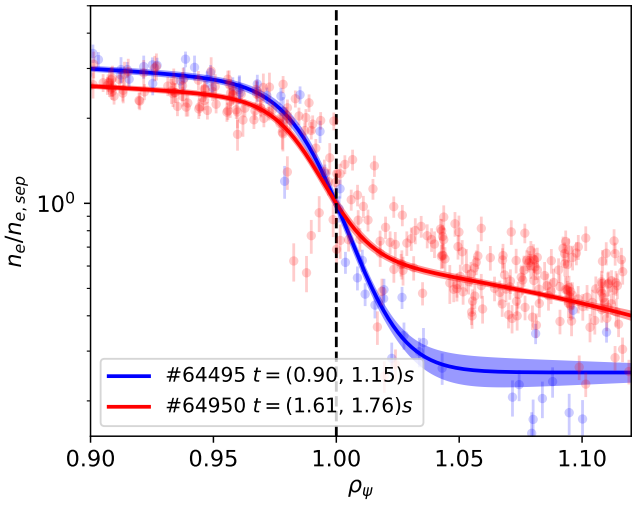

Figure 8: Upstream edge-SOL electron density profiles shown in figure 4, normalized to their respective separatrix density values. The vertical scale of the plot is logarithmic, for better visualization of the different shape of the two profiles as the divertor evolves towards a more dissipative state. The separatrix position has been represented through a dashed black vertical line.

any absolute difference in shape features. It can be seen that, as the separatrix density is raised at increasing divertor fuelling, the upstream density profile becomes flatter in the vicinity of the separatrix whereas in the far SOL a density shoulder is developed.

These two behaviours are well retained throughout all the present shots. The near-SOL density e-folding length λ_n has been evaluated by means of an exponential fit of data points within a 19 mm ($\sim 2\rho_{s,pol}$) wide interval along the radial coordinate, comprising part of the confined region, and afterwards mapped to its poloidal average $\langle\lambda_n\rangle$. On the other hand, in order to estimate the density shoulder amplitude the procedure described in [10] has been followed, in which the shoulder is characterised globally across both the near and far SOL by using the parameter

$$\tilde{n}_e = \frac{\int_0^{\Delta s} n_e ds}{n_{e,sep}\Delta s} = \frac{\langle n_e\rangle_{SOL}}{n_{e,sep}} \tag{9}$$

consisting of the ratio between the average SOL and separatrix densities; equation 4.2 has been evaluated at a depth $\Delta s = 35mm$ from the separatrix position into the SOL. As displayed in figure 9, both the near-SOL e-folding length and the density shoulder amplitude increase whenever the plasma becomes more resistive-interchange unstable near the separatrix as a consequence of growing divertor neutral pressure.

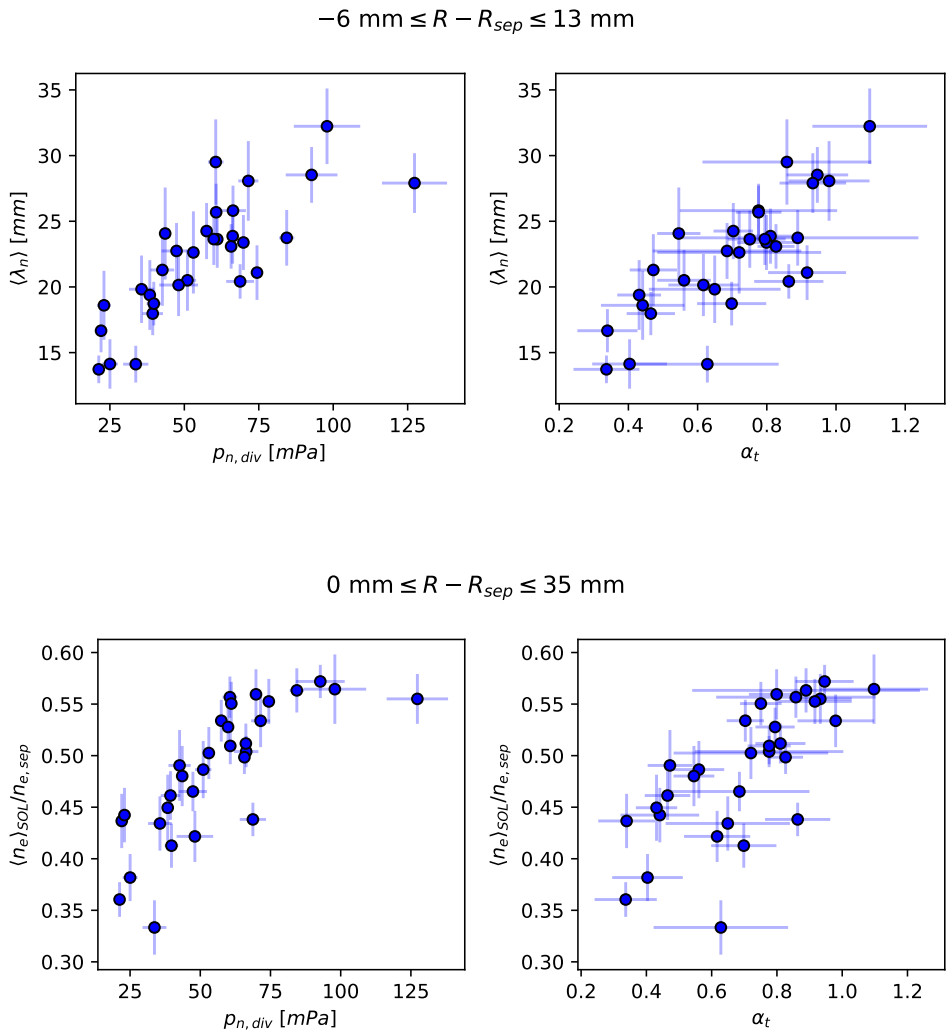

Figure 9: Evolution of the near-SOL density e-folding length (top panels) and density shoulder amplitude (bottom panels) with varying divertor neutral pressure and α_t parameter. The radial coordinate interval in which the considered quantities are evaluated are reported separately for the topo and bottom panels.

5. Role of filamentary transport

5.1. Filament parameters

In recent experimental activities the role of blob-filaments in the scrape-off layer has been identified as crucial in determining the general broadening of the SOL power load and density profiles with the associated formation of a density shoulder, particularly within QCE H-modes [13]. In the present contribution a preliminary evaluation of the filament properties has been carried out using the data provided by the midplane fast reciprocating probe, using the *conditional average sampling* (CAS) procedure described

in [33, 9]. Considering the RCP ion saturation current density signal J_{sat}, properly ELM-filtered when necessary, filaments have been detected as peaks higher than 2.5 standard deviations with respect to the signal moving average. The CAS procedure has been carried out during sub-intervals of the probe plunges of duration ranging from 3 to 8 ms according to the different ELM conditions, with the requirement of having sufficient blob statistics so as to get a robust evaluation of the filament properties. The average blob radius is defined as

$$\delta_b = \frac{\tau_b}{2}\sqrt{v_{b,r}^2 + v_{b,p}^2} \tag{10}$$

where τ_b is the FWHM of the conditionally averaged J_{sat} waveform, including possible effects linked to the presence of a trailing wake in the sample unlike what has been done in [33]. The filament radial velocity $v_{b,r}$ has been evaluated as the radial component of the $\mathbf{E} \times \mathbf{B}$ drift velocity exploiting the CAS of the poloidal electric field fluctuations calculated at the detection times of the J_{sat} peaks. The poloidal electric field is derived from the gradient of the floating potential between two poloidally-spaced electrodes on the probe head. The filament poloidal velocity $v_{b,p}$ has been instead estimated by using 2D cross-correlation techniques between all five floating potential pins, as described in [33]. The obtained blob sizes have been normalized to the local ion sound Larmor radius $\rho_s = \frac{\sqrt{M_i(\bar{Z}T_e+\gamma T_i)}}{eB}$, where the assumptions $\gamma \sim 1$ and $T_i = T_e$ have been used. Like in the previous sections, only points with uncertainty smaller than their absolute value have been taken into consideration. In addition to this, the present filament database has been further restricted to probe plunge sub-intervals whose average midplane radius is such that significant changes in connection length due to magnetic field line shadowing by the first wall are not considered, leading to an upper bound $\rho_\psi \lesssim 1.12$ (i.e. $R_{OMP} \leq 1.1376$ m in physical units) on the radial coordinate.

The results of this analysis are shown in figure 10, where the variation of each blob property has been assessed as a function of the turbulence control parameter and, by means of the color map, of the probe radial position in the SOL. The represented α_t values are those derived from evaluation of profile properties, performed in the previous sections, during time intervals entirely containing the reciprocating probe plunge. Despite the fact that the produced α_t range is narrower than in previous sections, significant variation in the filament properties can still be observed. In particular, in this analysis the blobs are seen to become bigger in size as α_t increases, mainly related to a corresponding increase of their radial propagation velocity by means of equation 10, while neither the FWHM of the filament waveforms nor the poloidal velocity show any clear trend. This observation is well in line with previous H-mode studies on ASDEX-Upgrade [17, 14] as well as a recent L-mode analysis on TCV [52] showing that a higher resistive-interchange turbulence activity close to the separatrix, resulting from an increase in gas fuelling and therefore separatrix collisionality, drives bigger and radially faster filaments to be expelled into the far SOL. Finally, in figure 10 it is also shown by means of the color map that the blob properties are substantially independent of their radial position across the scrape-off layer.

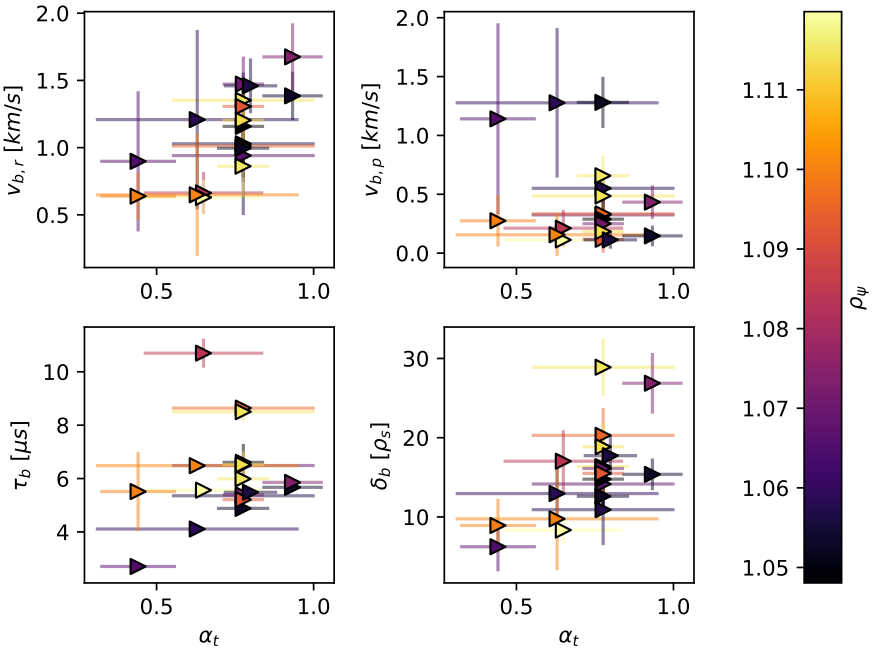

Figure 10: Dependence of filament properties on the α_t parameter, namely radial blob velocity $v_{b,r}$ (top left), poloidal blob velocity $v_{b,p}$ (top right), blob FWHM τ_b (bottom left) and blob radius δ_b (bottom right). Throughout the figures, the color map and the associated color bar on the right indicate the average position of the fast reciprocating probe across the SOL during the corresponding sub-intervals of the plunge.

5.2. Propagation regimes

In the following, the detected blobs are classified according to their regimes of propagation. These have been described within the well-known two-region model, first introduced in [53] and later extended in [54] in order to account for some blob non-idealities. In this model the drive for blob motion is provided by a balance between the charge separation stemming from ∇B and curvature drifts, and the electrical current flowing along the dominating current closure path. Within the two-region model the closure scheme, and thereby the propagation regime, depends on the relative value of the two invariants

$$\Lambda = \frac{\nu_{ei}}{\Omega_e \rho_s} L_\parallel \tag{11}$$

$$\Theta = \left(\frac{\delta_b R^{1/5}}{L_\parallel^{2/5} \rho_s^{4/5}} \right)^{5/2} \tag{12}$$

dubbed respectively normalised collisionality and normalised filament radius. At low collisionality and large radius filaments propagate within the *sheath-connected* regime (C_s), where the current path extends all the way to the divertor target and its magnitude is limited only by sheath resistivity. Conversely, at high collisionality and small

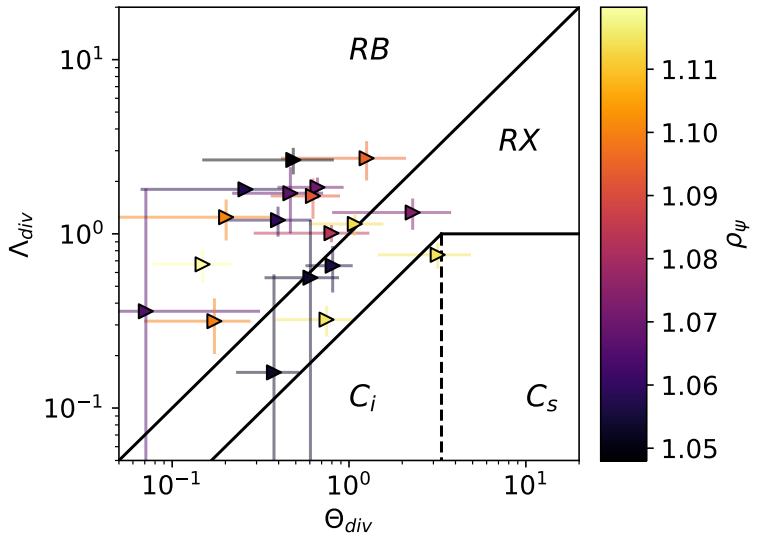

Figure 11: Dispersion plot of the detected CAS filament waveforms on the $\Lambda_{div} - \Theta_{div}$ plane. Both the horizontal and vertical scales are logarithmic for visualization purposes. The color map and the associated color bar represent the average position of the probe across the SOL during the corresponding plunge sub-interval. The continuous or dashed lines indicate the boundaries between different filament propagation regimes. In analogy to [33], the boundary between C_s and C_i regimes has been estimated at $\Theta_{div} \sim 1/0.3$.

size the *resistive ballooning* regime (RB) prevails, where the filaments are completely disconnected from the divertor target and their charge separation is drained primarily by the upstream cross-field ion polarisation current. In between these two extremes, for large collisionality and size propagation takes place within the *resistive X-point* regime (RX), with the interchange drive being balanced by parallel resistivity and filaments being only partially connected to the divertor region. Finally, in the *ideal-interchange* regime (C_i), dominating at small collisionality and size, the upstream curvature drive is balanced by the cross-field ion polarisation current in the divertor region, enhanced by flux expansion around the X-point.

The Λ parameter deserves particular attention, since it has been experimentally recognized to play a role in determining an enhancement of filamentary transport in L-mode high density scenarios [55, 56]. Notably, JET studies have shown that the dominant role in blob disconnection is played by the effective divertor collisionality Λ_{div} [56], defined from equation 11 by using divertor plasma quantities and the X-point-to-target connection length. Therefore, in figure 11 the parameter Λ_{div} is used in order to classify the detected blob waveforms according to their propagation regime, where the boundaries between them are also represented. Data from the floor Langmuir probes, namely density and temperature, have been taken as representative of the plasma conditions in the divertor region. For coherence, also the normalised size parameter is calculated as Θ_{div} by using the downstream connection length, whereas the

other quantities appearing in equation 12 are taken at the upstream filament detection location.

Coherently with the observations made in [33, 9], as displayed in figure 11 the detected blobs mainly belong to the RB and RX regimes of propagation, meaning that they are either marginally connected to the divertor target or, as in the majority of cases, completely disconnected; on the other hand, no relevant trend emerges on the radial coordinate. These observations seem to be supported by a recent preliminary analysis on wall-mounted Langmuir probes run at constant negative bias, in order to infer ion saturation current fluctuations with high time resolution, in conditions similar to those considered throughout this paper [14]. Indeed, in the mentioned work a progressive increase of the filament detection frequency has been found at increasing divertor neutral pressure from probes located at the outer midplane and at the LFS baffle tip, while no sensible variation has been detected from floor probes. This suggests that in the considered operating regimes the upstream filament behaviour may be substantially uncorrelated from the one taking place downstream near the divertor target.

6. Conclusions

An extensive experimental effort has been carried out on the TCV tokamak within the most recent EUROfusion tokamak exploitation work packages with the aim of studying the effect of varying gas fuelling on the properties of upstream SOL profiles and turbulence in high-density H-mode scenario. By varying the fuelling rate in the toroidal chamber, a wide scan in divertor neutral pressure has been achieved at constant plasma current, toroidal field and poloidal magnetic equilibrium. A transition of the ELM behaviour has been seen at increasing divertor fuelling from well defined large type-I bursts towards a QCE regime with lower amplitude and markedly incoherent fluctuations, substantially recovering previous experimental observations [15, 16, 13]. The increase of divertor neutral pressure has been linked, via higher separatrix density, to a growing resistive interchange turbulence activity close to the separatrix by means of the α_t turbulence control parameter [1]. The upstream SOL profiles undergo a significant modification according to the evolution of the divertor recycling state. More specifically, in the near SOL the enhanced resistive turbulence level near the separatrix determines a widening of the power channel with a corresponding reduction of the peak heat load. In the same way, the near SOL density e-folding length has been found to increase significantly, up to a factor ~ 2.5 across the spanned α_t interval. In the far SOL the development of a density shoulder feature, similarly to L-mode conditions, is seen as a direct consequence of the enhanced resistive ballooning turbulence associated to a higher separatrix collisionality. In the considered experiments the latter takes the form of a more intense filamentary activity, with clear evidence of bigger blobs travelling faster along the outward radial direction across the far SOL. The detected filaments have been mapped on the $\Lambda_{div} - \Theta_{div}$ parameter space within the two-region model, revealing that their radial propagation is mostly consistent with disconnected regimes, namely RX and

RB. It is important to stress how the present analysis of filamentary transport is still at a preliminary stage, relying on workflows adopted in previous L-mode analysis [33, 9] and being affected by some limitations due to the point-like nature of the reciprocating probe measurements or the lack of a method to evaluate independently the blob size and velocity. Despite this, the obtained results allow to build a physically sound picture of the link between the enhancement of resistive ballooning transport and the behaviour of the upstream profiles in the examined scenario.

It must be noted that the density dependence, controlled to some degree by the divertor neutral pressure, is only one among many others appearing in equation 3. This opens up the possibility of probing different parameter dependencies, for instance the machine size dependence through the tokamak major radius allows for a direct comparison between different devices. Potentially, a unified description of the properties of SOL profiles and transport among different tokamaks could be provided solely through the α_t parameter. Moreover, plasma shaping has been already demonstrated to be key in controlling the ELM regime by modifying the magnetic shear around the outer midplane [15, 16], therefore for future work an extension of the present analysis is foreseen so as to include the effect of varying shaping parameters (e.g. the upper triangularity).

Acknowledgments

This work has been carried out within the framework of the EUROfusion Consortium, funded by the European Union via the Euratom Research and Training Programme (Grant Agreement No 101052200 — EUROfusion). Views and opinions expressed are however those of the author(s) only and do not necessarily reflect those of the European Union or the European Commission. Neither the European Union nor the European Commission can be held responsible for them. This work was supported in part by the Swiss National Science Foundation and in part by the US Department of Energy under award No. DE-SC0010529.

References

[1] Eich T, Manz P, Goldston R, Hennequin P, David P, Faitsch M, Kurzan B, Sieglin B and Wolfrum E 2020 *Nuclear Fusion* **60** 056016

[2] Pitts R, Bonnin X, Escourbiac F, Frerichs H, Gunn J, Hirai T, Kukushkin A, Kaveeva E, Miller M, Moulton D, Rozhansky V, Senichenkov I, Sytova E, Schmitz O, Stangeby P, De Temmerman G, Veselova I and Wiesen S 2019 *Nuclear Materials and Energy* **20** 100696 ISSN 2352-1791

[3] Sips A, Schweinzer J, Luce T, Wolfe S, Urano H, Hobirk J, Ide S, Joffrin E, Kessel C, Kim S, Lomas P, Nunes I, Pütterich T, Rimini F, Solomon W, Stober J, Turco F, de Vries P, , , , and and 2018 *Nuclear Fusion* **58** 126010

[4] Kallenbach A, Bernert M, Dux R, Eich T, Henderson S, Pütterich T, Reimold F, Rohde V and Sun H 2019 *Nuclear Materials and Energy* **18** 166–174 ISSN 2352-1791

[5] LaBombard B, Boivin R L, Greenwald M, Hughes J, Lipschultz B, Mossessian D, Pitcher C S, Terry J L and Zweben S J 2001 *Physics of Plasmas* **8** 2107–2117

[6] Rudakov D, Boedo J, Moyer R, Stangeby P, Watkins J, Whyte D, Zeng L, Brooks N, Doerner R, Evans T, Fenstermacher M, Groth M, Hollmann E, Krasheninnikov S, Lasnier C, Leonard A,

Mahdavi M, McKee G, McLean A, Pigarov A, Wampler W, Wang G, West W and Wong C 2005 *Nuclear Fusion* **45** 1589–1599

[7] Garcia O, Horacek J, Pitts R, Nielsen A, Fundamenski W, Naulin V and Rasmussen J J 2007 *Nuclear Fusion* **47** 667–676

[8] Carralero D, Artene S, Bernert M, Birkenmeier G, Faitsch M, Manz P, de Marne P, Stroth U, Wischmeier M, Wolfrum E and and 2018 *Nuclear Fusion* **58** 096015

[9] Vianello N, Carralero D, Tsui C, Naulin V, Agostini M, Cziegler I, Labit B, Theiler C, Wolfrum E, Aguiam D, Allan S, Bernert M, Boedo J, Costea S, Oliveira H D, Fevrier O, Galdon-Quiroga J, Grenfell G, Hakola A, Ionita C, Isliker H, Karpushov A, Kovacic J, Lipschultz B, Maurizio R, McClements K, Militello F, Nielsen A, Olsen J, Rasmussen J, Ravensbergen T, Reimerdes H, Schneider B, Schrittwieser R, Seliunin E, Spolaore M, Verhaegh K, Vicente J, Walkden N, Zhang W, and and 2020 *Nuclear Fusion* **60** 016001

[10] Février O, Theiler C, Harrison J R, Tsui C K, Verhaegh K, Wüthrich C, Boedo J A, Oliveira H D, Duval B P, Labit B, Lipschultz B, Maurizio R, Reimerdes H and and 2020 *Plasma Physics and Controlled Fusion* **62** 035017

[11] Müller H, Bernert M, Carralero D, Kallenbach A, Kurzan B, Scarabosio A, Sieglin B, Tophøj L, Vianello N and Wolfrum E 2015 *Journal of Nuclear Materials* **463** 739–743 ISSN 0022-3115 pLASMA-SURFACE INTERACTIONS 21

[12] Carralero D, Madsen J, Artene S, Bernert M, Birkenmeier G, Eich T, Fuchert G, Laggner F, Naulin V, Manz P, Vianello N and Wolfrum E 2017 *Nuclear Materials and Energy* **12** 1189–1193 ISSN 2352-1791 proceedings of the 22nd International Conference on Plasma Surface Interactions 2016, 22nd PSI

[13] Faitsch M, Eich T, Harrer G, Wolfrum E, Brida D, David P, Griener M, Stroth U, Team T A U and Team T E M 2021 *Nuclear Materials and Energy* **26** 100890 ISSN 2352-1791

[14] Vianello N, Walkden N, Dunne M, Lomanowski B, Wolfrum E, Tsui C, Stagni A, Griener M, Tal B, Eich T, Refy D, Brida D, Février O, Agostini M, Oliveira H D, Aleiferis S, Bernert M, Boedo J, Brix M, Carralero D, Carvalho I, Falchetto G, Frassinetti L, Giroud C, Hakola A, Huber A, Karhunen J, Karpushov A, Labit B, Meigs A, Naulin V, Pereira T, Thun C P V, Reimerdes H, Gorno S, Theiler C, the ASDEX Upgrade team, the TCV team, the EUROfusion MST1 team and the JET Contributors 10-15 May 2021 SOL profile and fluctuations in different divertor recycling conditions in H-mode plasmas *Proc. 28th IAEA Fusion Energy Conference* (Nice, France (Remote)) URL https://nucleus.iaea.org/sites/fusionportal/Shared%20Documents/FEC%202020/fec2020-preprints/preprint1051.pdf

[15] Harrer G, Wolfrum E, Dunne M, Manz P, Cavedon M, Lang P, Kurzan B, Eich T, Labit B, Stober J, Meyer H, Bernert M, Laggner F, Aumayr F and and 2018 *Nuclear Fusion* **58** 112001

[16] Labit B, Eich T, Harrer G, Wolfrum E, Bernert M, Dunne M, Frassinetti L, Hennequin P, Maurizio R, Merle A, Meyer H, Saarelma S, Sheikh U, Adamek J, Agostini M, Aguiam D, Akers R, Albanese R, Albert C, Alessi E, Ambrosino R, Andrèbe Y, Angioni C, Apruzzese G, Aradi M, Arnichand H, Auriemma F, Avdeeva G, Ayllon-Guerola J, Bagnato F, Bandaru V, Barnes M, Barrera-Orte L, Bettini P, Bilato R, Biletskyi O, Bilkova P, Bin W, Blanchard P, Blanken T, Bobkov V, Bock A, Boeyaert D, Bogar K, Bogar O, Bohm P, Bolzonella T, Bombarda F, Boncagni L, Bouquey F, Bowman C, Brezinsek S, Brida D, Brunetti D, Bucalossi J, Buchanan J, Buermans J, Bufferand H, Buller S, Buratti P, Burckhart A, Calabrò G, Calacci L, Camenen Y, Cannas B, Megías P C, Carnevale D, Carpanese F, Carr M, Carralero D, Carraro L, Casolari A, Cathey A, Causa F, Cavedon M, Cecconello M, Ceccuzzi S, Cerovsky J, Chapman S, Chmielewski P, Choi D, Cianfarani C, Ciraolo G, Coda S, Coelho R, Colas L, Colette D, Cordaro L, Cordella F, Costea S, Coster D, Zabala D C, Cseh G, Czarnecka A, Cziegler I, D'Arcangelo O, Molin A D, David P, Carolis G D, Oliveira H D, Decker J, Dejarnac R, Delogu R, den Harder N, Dimitrova M, Dolizy F, Durán J D P, Douai D, Drenik A, Dreval M, Dudson B, Dunai D, Duval B, Dux R, Elmore S, Embréus O, Erdõs B, Fable E, Faitsch M, Fanni A, Farnik M, Faust I, Faustin J, Fedorczak N, Felici F, Feng S, Feng X, Ferreira J, Ferrò G, Février O, Ficker O,

Figini L, Figueiredo A, Fil A, Fontana M, Francesco M, Fuchs C, Futatani S, Gabellieri L, Gadariya D, Gahle D, Galassi D, Gałązka K, Galdon-Quiroga J, Galeani S, Gallart D, Gallo A, Galperti C, Garavaglia S, Garcia J, Garcia-Lopez J, Garcia-Muñoz M, Garzotti L, Gath J, Geiger B, Giacomelli L, Giannone L, Gibson S, Gil L, Giovannozzi E, Giruzzi G, Gobbin M, Gonzalez-Martin J, Goodman T, Gorini G, Gospodarczyk M, Granucci G, Grekov D, Grenfell G, Griener M, Groth M, Grover O, Gruca M, Gude A, Guimarais L, Gyergyek T, Hacek P, Hakola A, Ham C, Happel T, Harrison J, Havranek A, Hawke J, Henderson S, Hesslow L, Hitzler F, Hnat B, Hobirk J, Hoelzl M, Hogeweij D, Hopf C, Hoppe M, Horacek J, Hron M, Huang Z, Iantchenko A, Iglesias D, Igochine V, Innocente P, Ionita-Schrittwieser C, Isliker H, Ivanova-Stanik I, Jacobsen A, Jakubowski M, Janky F, Jardin A, Jaulmes F, Jensen T, Jonsson T, Kallenbach A, Kappatou A, Karpushov A, Kasilov S, Kazakov Y, Kazantzidis P, Keeling D, Kelemen M, Kendl A, Kernbichler W, Kirk A, Kocsis G, Komm M, Kong M, Korovin V, Koubiti M, Kovacic J, Krawczyk N, Krieger K, Kripner L, Křivská A, Kudlacek O, Kulyk Y, Kurki-Suonio T, Kwiatkowski R, Laggner F, Laguardia L, Lahtinen A, Lang P, Likonen J, Lipschultz B, Liu F, Lombroni R, Lorenzini R, Loschiavo V, Lunt T, Macusova E, Madsen J, Maggiora R, Maljaars B, Manas P, Mantica P, Mantsinen M, Manz P, Maraschek M, Marchenko V, Marchetto C, Mariani A, Marini C, Markovic T, Marrelli L, Martin P, Solís J M, Martitsch A, Mastrostefano S, Matos F, Matthews G, Mayoral M L, Mazon D, Mazzotta C, Carthy P M, McClements K, McDermott R, Mcmillan B, Meineri C, Menkovski V, Meshcheriakov D, Messmer M, Micheletti D, Milanesio D, Militello F, Miron I, Mlynar J, Moiseenko V, Cabrera P M, Morales J, Moret J M, Moro A, Moulton D, Nabais F, Naulin V, Naydenkova D, Nem R, Nespoli F, Newton S, Nielsen A, Nielsen S, Nikolaeva V, Nocente M, Nowak S, Oberkofler M, Ochoukov R, Ollus P, Olsen J, Omotani J, Ongena J, Orain F, Orsitto F, Paccagnella R, Palha A, Panaccione L, Panek R, Panjan M, Papp G, Perez I P, Parra F, Passeri M, Pau A, Pautasso G, Pavlichenko R, Perek A, Radolfini V P, Pesamosca F, Peterka M, Petrzilka V, Piergotti V, Pigatto L, Piovesan P, Piron C, Piron L, Plyusnin V, Pokol G, Poli E, Pölöskei P, Popov T, Popovic Z, Pór G, Porte L, Pucella G, Puiatti M, Pütterich T, Rabinski M, Rasmussen J J, Rasmussen J, Rattá G, Ratynskaia S, Ravensbergen T, Réfy D, Reich M, Reimerdes H, Reimold F, Reiser D, Reux C, Reznik S, Ricci D, Rispoli N, Rivero-Rodriguez J, Rocchi G, Rodriguez-Ramos M, Romano A, Rosato J, Rubinacci G, Rubino G, Ryan D, Salewski M, Salmi A, Samaddar D, Sanchis-Sanchez L, Santos J, Särkimäki K, Sassano M, Sauter O, Scannell R, Scheffer M, Schneider B, Schneider P, Schrittwieser R, Schubert M, Seidl J, Seliunin E, Sharapov S, Sheeba R, Sias G, Sieglin B, Silva C, Sipilä S, Smith S, Snicker A, Solano E, Hansen S, Soria-Hoyo C, Sorokovoy E, Sozzi C, Sperduti A, Spizzo G, Spolaore M, Stejner M, Stipani L, Stober J, Strand P, Sun H, Suttrop W, Sytnykov D, Szepesi T, Tál B, Tala T, Tardini G, Tardocchi M, Teplukhina A, Terranova D, Testa D, Theiler C, Thorén E, Thornton A, Tilia B, Tolias P, Tomes M, Toscano-Jimenez M, Tsironis C, Tsui C, Tudisco O, Urban J, Valisa M, Vallar M, Olivares P V, Valovic M, Vugt D V, Vanovac B, Varje J, Varju J, Varoutis S, Vartanian S, Vasilovici O, Vega J, Verdoolaege G, Verhaegh K, Vermare L, Vianello N, Vicente J, Viezzer E, Villone F, Voitsekhovitch I, Voltolina D, Vondracek P, Vu N, Walkden N, Wauters T, Weiland M, Weinzettl V, Wensing M, Wiesen S, Wiesenberger M, Wilkie G, Willensdorfer M, Wischmeier M, Wu K, Xiang L, Zagorski R, Zaloga D, Zanca P, Zaplotnik R, Zebrowski J, Zhang W, Zisis A, Zoletnik S and Zuin M 2019 *Nuclear Fusion* **59** 086020

[17] Griener M, Wolfrum E, Birkenmeier G, Faitsch M, Fischer R, Fuchert G, Gil L, Harrer G, Manz P, Wendler D and Stroth U 2020 *Nuclear Materials and Energy* **25** 100854 ISSN 2352-1791

[18] D'Ippolito D A, Myra J R and Zweben S J 2011 *Physics of Plasmas* **18** 060501

[19] Rogers B N, Drake J F and Zeiler A 1998 *Phys. Rev. Lett.* **81**(20) 4396–4399

[20] Scott B D 2005 *Physics of Plasmas* **12** 062314

[21] Scott B D 2007 *Plasma Physics and Controlled Fusion* **49** S25–S41

[22] Scott B D 2002 *New Journal of Physics* **4** 52–52

[23] Reimerdes H, Agostini M, Alessi E, Alberti S, Andrebe Y, Arnichand H, Balbin J, Bagnato F,

Baquero-Ruiz M, Bernert M, Bin W, Blanchard P, Blanken T, Boedo J, Brida D, Brunner S, Bogar C, Bogar O, Bolzonella T, Bombarda F, Bouquey F, Bowman C, Brunetti D, Buermans J, Bufferand H, Calacci L, Camenen Y, Carli S, Carnevale D, Carpanese F, Causa F, Cavalier J, Cavedon M, Cazabonne J, Cerovsky J, Chandra R, Jayalekshmi A C, Chellaï O, Chmielewski P, Choi D, Ciraolo G, Classen I, Coda S, Colandrea C, Molin A D, David P, de Baar M, Decker J, Dekeyser W, de Oliveira H, Douai D, Dreval M, Dunne M, Duval B, Elmore S, Embreus O, Eriksson F, Faitsch M, Falchetto G, Farnik M, Fasoli A, Fedorczak N, Felici F, Février O, Ficker O, Fil A, Fontana M, Fransson E, Frassinetti L, Furno I, Gahle D, Galassi D, Galazka K, Galperti C, Garavaglia S, Garcia-Munoz M, Geiger B, Giacomin M, Giruzzi G, Gobbin M, Golfinopoulos T, Goodman T, Gorno S, Granucci G, Graves J, Griener M, Gruca M, Gyergyek T, Haelterman R, Hakola A, Han W, Happel T, Harrer G, Harrison J, Henderson S, Hogeweij G, Hogge J P, Hoppe M, Horacek J, Huang Z, Iantchenko A, Innocente P, Björk K I, Ionita-Schrittweiser C, Isliker H, Jardin A, Jaspers R, Karimov R, Karpushov A, Kazakov Y, Komm M, Kong M, Kovacic J, Krutkin O, Kudlacek O, Kumar U, Kwiatkowski R, Labit B, Laguardia L, Lammers J, Laribi E, Laszynska E, Lazaros A, Linder O, Linehan B, Lipschultz B, Llobet X, Loizu J, Lunt T, Macusova E, Marandet Y, Maraschek M, Marceca G, Marchetto C, Marchioni S, Marmar E, Martin Y, Martinelli L, Matos F, Maurizio R, Mayoral M L, Mazon D, Menkovski V, Merle A, Merlo G, Meyer H, Mikszuta-Michalik K, Cabrera P M, Morales J, Moret J M, Moro A, Moulton D, Muhammed H, Myatra O, Mykytchuk D, Napoli F, Nem R, Nielsen A, Nocente M, Nowak S, Offeddu N, Olsen J, Orsitto F, Pan O, Papp G, Pau A, Perek A, Pesamosca F, Peysson Y, Pigatto L, Piron C, Poradzinski M, Porte L, Pütterich T, Rabinski M, Raj H, Rasmussen J, Rattá G, Ravensbergen T, Ricci D, Ricci P, Rispoli N, Riva F, Rivero-Rodriguez J, Salewski M, Sauter O, Schmidt B, Schrittweiser R, Sharapov S, Sheikh U, Sieglin B, Silva M, Smolders A, Snicker A, Sozzi C, Spolaore M, Stagni A, Stipani L, Sun G, Tala T, Tamain P, Tanaka K, Biwole A T, Terranova D, Terry J, Testa D, Theiler C, Thornton A, Thrysøe A, Torreblanca H, Tsui C, Vaccaro D, Vallar M, van Berkel M, Eester D V, van Kampen R, Mulders S V, Verhaegh K, Verhaeghe T, Vianello N, Villone F, Viezzer E, Vincent B, Voitsekhovitch I, Vu N, Walkden N, Wauters T, Weisen H, Wendler N, Wensing M, Widmer F, Wiesen S, Wischmeier M, Wijkamp T, Wünderlich D, Wüthrich C, Yanovskiy V, Zebrowski J and the EUROfusion MST1 Team 2022 *Nuclear Fusion* **62** 042018

[24] Fasoli A, Reimerdes H, Alberti S, Baquero-Ruiz M, Duval B, Havlikova E, Karpushov A, Moret J M, Toussaint M, Elaian H, Silva M, Theiler C and and D V 2019 *Nuclear Fusion* **60** 016019

[25] Reimerdes H, Duval B, Elaian H, Fasoli A, Février O, Theiler C, Bagnato F, Baquero-Ruiz M, Blanchard P, Brida D, Colandrea C, Oliveira H D, Galassi D, Gorno S, Henderson S, Komm M, Linehan B, Martinelli L, Maurizio R, Moret J M, Perek A, Raj H, Sheikh U, Testa D, Toussaint M, Tsui C, Wensing M, the TCV team and the EUROfusion MST1 team 2021 *Nuclear Fusion* **61** 024002

[26] Bates S C and Burrell K H 1984 *Review of Scientific Instruments* **55** 934–939

[27] Hawke J, Andrebe Y, Bertizzolo R, Blanchard P, Chavan R, Decker J, Duval B, Lavanchy P, Llobet X, Marlétaz B, Marmillod P, Pochon G and Toussaint M 2017 *Journal of Instrumentation* **12** C12005–C12005

[28] Furno I, Weisen H, Mlynar J, Pitts R A, Llobet X, Marmillod P and Pochon G P 1999 *Review of Scientific Instruments* **70** 4552–4556

[29] Maurizio R, Elmore S, Fedorczak N, Gallo A, Reimerdes H, Labit B, Theiler C, Tsui C, Vijvers W and and 2018 *Nuclear Fusion* **58** 016052

[30] Février O, Theiler C, De Oliveira H, Labit B, Fedorczak N and Baillod A 2018 *Review of Scientific Instruments* **89** 053502

[31] De Oliveira H, Marmillod P, Theiler C, Chavan R, Février O, Labit B, Lavanchy P, Marlétaz B and Pitts R A 2019 *Review of Scientific Instruments* **90** 083502

[32] Boedo J 2009 *Journal of Nuclear Materials* **390-391** 29–37 ISSN 0022-3115 proceedings of the 18th International Conference on Plasma-Surface Interactions in Controlled Fusion Device

[33] Tsui C K, Boedo J A, Myra J R, Duval B, Labit B, Theiler C, Vianello N, Vijvers W A J, Reimerdes H, Coda S, Février O, Harrison J R, Horacek J, Lipschultz B, Maurizio R, Nespoli F, Sheikh U, Verhaegh K and Walkden N 2018 *Physics of Plasmas* **25** 072506
[34] Karpushov A N, Chavan R, Coda S, Davydenko V I, Dolizy F, Dranitchnikov A N, Duval B P, Ivanov A A, Fasel D, Fasoli A, Kolmogorov V V, Lavanchy P, Llobet X, Marlétaz B, Marmillod P, Martin Y, Merle A, Perez A, Sauter O, Siravo U, Shikhovtsev I V, Sorokin A V and Toussaint M 2017 *Fusion Engineering and Design* **123** 468–472
[35] Greenwald M, Terry J, Wolfe S, Ejima S, Bell M, Kaye S and Neilson G 1988 *Nuclear Fusion* **28** 2199–2207
[36] Moret J M, Duval B, Le H, Coda S, Felici F and Reimerdes H 2015 *Fusion Engineering and Design* **91** 1–15 ISSN 0920-3796
[37] Groebner R, Baker D, Burrell K, Carlstrom T, Ferron J, Gohil P, Lao L, Osborne T, Thomas D, West W, Boedo J, Moyer R, McKee G, Deranian R, Doyle E, Rettig C, Rhodes T and Rost J 2001 *Nuclear Fusion* **41** 1789–1802
[38] Rovere E 2019 *Development of the EUROfusion pedestal database for ELMy H-Mode for the TCV tokamak* Master's thesis Politecnico di Milano Milano, Italy URL http://hdl.handle.net/10589/145958
[39] Stangeby P, Canik J, Elder J, Lasnier C, Leonard A, Eldon D, Makowski M, Osborne T and Grierson B 2015 *Nuclear Fusion* **55** 093014
[40] Eich T, Sieglin B, Scarabosio A, Fundamenski W, Goldston R J and Herrmann A (ASDEX Upgrade Team) 2011 *Phys. Rev. Lett.* **107**(21) 215001
[41] Goldston R J, Reinke M L and Schwartz J A 2017 *Plasma Physics and Controlled Fusion* **59** 055015
[42] Sauter O, Angioni C and Lin-Liu Y R 1999 *Physics of Plasmas* **6** 2834–2839
[43] Sauter O, Angioni C and Lin-Liu Y R 2002 *Physics of Plasmas* **9** 5140–5140
[44] Sheikh U A, Dunne M, Frassinetti L, Blanchard P, Duval B P, Labit B, Merle A, Sauter O, Theiler C, Tsui C and and 2018 *Plasma Physics and Controlled Fusion* **61** 014002
[45] Herrmann A, Junker W, Gunther K, Bosch S, Kaufmann M, Neuhauser J, Pautasso G, Richter T and Schneider R 1995 *Plasma Physics and Controlled Fusion* **37** 17–29
[46] Sieglin B, Faitsch M, Herrmann A, Brucker B, Eich T, Kammerloher L and Martinov S 2015 *Review of Scientific Instruments* **86** 113502
[47] Maurizio R, Duval B, Elmore S, Fedorczak N, Labit B, Nespoli F, Reimerdes H, Sheikh U and Theiler C 4-8 July 2016 Infrared measurements of the heat flux spreading under variable divertor geometries in TCV *Proc. 43rd EPS Conference on Plasma Physics* (Leuven, Belgium) URL http://ocs.ciemat.es/EPS2016PAP/pdf/P4.027.pdf
[48] Eich T, Leonard A, Pitts R, Fundamenski W, Goldston R, Gray T, Herrmann A, Kirk A, Kallenbach A, Kardaun O, Kukushkin A, LaBombard B, Maingi R, Makowski M, Scarabosio A, Sieglin B, Terry J, Thornton A and and 2013 *Nuclear Fusion* **53** 093031
[49] Goldston R 2012 *Nuclear Fusion* **52** 013009
[50] Goldston R 2015 *Journal of Nuclear Materials* **463** 397–400 ISSN 0022-3115 pLASMA-SURFACE INTERACTIONS 21
[51] Maurizio R, Duval B, Labit B, Reimerdes H, Faitsch M, Komm M, Sheikh U, Theiler C and the TCV team 2021 *Nuclear Fusion* **61** 024003
[52] Offeddu N, Han W, Theiler C, Golfinopoulos T, Terry J, Marmar E, Wüthrich C, Tsui C, de Oliveira H, Duval B, Galassi D, de Oliveira D and Mancini D 2022 Cross-field and parallel dynamics of SOL filaments in TCV submitted to *Nucl. Fusion*
[53] Myra J R, Russell D A and D'Ippolito D A 2006 *Physics of Plasmas* **13** 112502
[54] Paruta P, Beadle C, Ricci P and Theiler C 2019 *Physics of Plasmas* **26** 032302
[55] Carralero D, Manz P, Aho-Mantila L, Birkenmeier G, Brix M, Groth M, Müller H W, Stroth U, Vianello N and Wolfrum E (ASDEX Upgrade team and JET Contributors and EUROfusion MST1 Team) 2015 *Phys. Rev. Lett.* **115**(21) 215002

[56] Carralero D, Müller H, Groth M, Komm M, Adamek J, Birkenmeier G, Brix M, Janky F, Hacek P, Marsen S, Reimold F, Silva C, Stroth U, Wischmeier M and Wolfrum E 2015 *Journal of Nuclear Materials* **463** 123–127 ISSN 0022-3115 pLASMA-SURFACE INTERACTIONS 21